Monitoring of industrial crystallization processes through image sequence segmentation and characterization

Saïd Rahmani, Roger de Souza Lima, Eric Serris, Ana Cameirão, Johan Debayle

Monitoring of Industrial Crystallization Processes through Image Sequence Segmentation and Characterization

Saïd Rahmani[a,*], **Roger de Souza Lima**[a], **Eric Serris**[a], **Ana Cameirão**[a], **Johan Debayle**[a]
[a]Ecole Nationale Supérieure des Mines Saint-Étienne, Univ Lyon, CNRS, UMR 5307, Centre SPIN, F – 42023 Saint-Etienne, France.

Abstract.
To enhance control and monitoring of industrial crystallization processes, we propose an innovative non-destructive imaging method utilizing *in-situ* 2D vision sensors. This approach enables the acquisition of 2D videos depicting crystal aggregates throughout the batch crystallization process. Our approach is built upon experimental observations, specifically regarding the process dynamics and sensor fouling. It involves dynamic segmentation of observed aggregates, from which quantitative analyses are derived. Notably, our method allows for tracking the evolution of the particle size distribution (PSD) of crystal aggregates over time and the determination of the growth kinetics of crystals that agglomerate at the sensor air gap. This enables the detection of key stages in the crystallization process and the geometric characterization of crystal aggregate production.

Keywords: Batch crystallization process, Crystal growth kinetics, Dynamic video segmentation, *in-situ* 2D vision sensors, Industrial crystallizers, Particle size distribution..

***Contact author:** said.rahmani@emse.fr

1 Introduction

This paper is devoted to develop an image analysis method for the monitoring of industrial crystallisation process. It is a part of a global framework with the goal of revolutionizing the operation and maintenance of both batch and continuous industrial crystallizers through digital technology and innovative sensor technologies. The project employs various on-line sensors, including acoustic emission[1,2] and imaging, placed within the reactor to provide real-time quantitative data on crystallization. This data is used for monitoring the characteristics of the crystalline population, including crystallization kinetics, crystal morphology, and quantity.[3,4]

This online multi-sensor monitoring system facilitates the precise adjustment of operational parameters for optimizing output and better control over crystal production. Ultimately, these digital tools hold promise for addressing a range of industrial challenges, such as quality control and

incident prevention (e.g., pipe blockages).[5]

1.1 Motivation

Real-time video imaging facilitates the direct observation of crystallization processes within the reactor, offering numerous advantages. It enables *in-situ* process monitoring while providing rich information about crystal morphology through 2D projections of crystal aggregates. Regarding the monitoring of crystallization processes, the expectations for analysing videos from an *in-situ* probe are diverse. The primary objective is to obtain quantitative information regarding the number, size, and shape of crystals/aggregates in the reactor (particle size distribution) at each time.[6] In fact, there are few *in-situ* alternatives to image analysis for obtaining such information.

However, several constraints arise in the analysis of these images. The tools implemented must be sufficiently robust and generic to handle various types of crystals with highly variable morphologies. Furthermore, these tools must be capable of processing images with varying crystal densities, including the rather problematic case of high density due to probe fouling (see below). Actually, analysing such images can be exceptionally challenging, especially when crystal density is high. The variability in crystal morphology, with crystals often appearing superimposed, agglomerated, shiny, or transparent, complicates identification. This complexity has prompted extensive research and the development of various specialized image analysis techniques.

1.2 Related works

From an image analysis perspective, characterizing crystals presents several intricate challenges. These include addressing issues related to characterizing a population of overlapping particles, dealing with the segmentation of complex images, and exploring aspects of projective stereology (characterizing 3D objects through their projections).[7,8] To characterize crystals, various approaches are employed, ranging from techniques that provide a more or less detailed characterization of aggregates (groups of crystals) to individual crystals.

However, there is a notable absence of a sufficiently robust method for characterizing crystals comprehensively in a generic framework, especially when dealing with different crystal types and variable densities. To address this gap, numerous techniques tailored to specific types of crystals and experimental situations have been developed. For instance, there are specific methods for L-glutamic acid,[9,10] for ammonium oxalate crystals,[11,12] or for citric acid.[13,14]

It should be noted that there are more generic techniques that enable coarse indirect characterization of object populations, such as morpho-granulometric analysis.[15,16] This tool serves as a robust means for the rough characterization of a population of crystals. Nevertheless, it falls short when it comes to providing a detailed description. Hence, we turn to specific pattern recognition methods. These methods typically involve making assumptions about the morphology of the objects and/or the overlap of the crystals. For instance, there are specific methods for overlapping polygonal-shaped crystals,[17] for crystal morphology identification of L-glutamic acid,[9,18,19] or for convex crystals assuming some knowledge about the intensity of the overlap.[20] Further-

more, the techniques employed often face limitations when dealing with particularly high crystal densities. However, it's worth noting the existence of methods tailored to high crystal densities of L-glutamic acid.[21,22] Some stereological approaches (inferring the 3D geometry of objects from their 2D projection) aimed at characterizing the 3D geometry of crystals have been developed;[7,23] nevertheless, they remain highly constrained in practice concerning the morphology of crystals. Furthermore, we should highlight innovative and highly promising stochastic geometry model-based methods.[24–27] These approaches propose addressing the disordered and unpredictable nature of crystal populations as a random phenomenon. Nevertheless, the current state of knowledge on the subject imposes heavy assumptions that restrict our ability to grasp the complexity of our data.

It's worth noting the presence of artificial intelligence-based methods to tackle similar problems. For instance, the Mask R-CNN[28] is widely used for object detection and semantic segmentation in images, providing precise delineation of object boundaries. Similarly, the StarDist method[29,30] has proven effectiveness in tasks such as segmentation of overlapping nuclei in microscopy images. While deep learning approaches are highly efficient and particularly suited for such problems, a major constraint remains: the demand for a substantial and representative ground-truth database during the training phase. Unfortunately, building such a ground truth database is not realistic in our case. Due to the complexity and diversity of the considered situations, it would require experts to manually segment thousands of images across various experimental configurations. This represents one of the main difficulties in our problem: the absence of a comprehensive ground-truth database. Consequently, we are unable to quantitatively evaluate the performance of our segmentations and characterizations, relying instead on visual inspection.

1.3 Outline of the paper

Given the unique challenges encountered in our industrial context, such as the morphological diversity of different types of crystals, probe fouling, high crystal density, and the lack of ground truth, it appears that methods from the literature may not be suitable for addressing our problem. Indeed, a review of the literature reveals, on one hand, the existence of coarse, generic but indirect and imprecise characterization methods, and on the other hand, the existence of fine-grained characterization methods that are highly specific to given situations. With the exception of deep learning techniques, which are not applicable due to the lack of ground truth, no method seems to exist that is sufficiently precise and general to address our issue.

In light of this, we have implemented an aggregate-scale characterization method, specific to our video acquisition system and tailored to the encountered fouling issues, while still being sufficiently generic to adapt to any type of crystal. The significance of this method lies in its versatility and its adaptation to the phenomena observed with our experimental setup.

Initially, we will introduce the specifics of our experimental setup, followed by a discussion of the nature and peculiarities of our acquisitions. Then, we will proceed to present the dynamic video segmentation method we have developed. Finally, this dynamic segmentation will be leveraged to obtain quantitative information on crystallization over time (particle size distribution, crystal growth kinetics).

To enhance the readability of the paper, the image analysis method proposed will be illustrated

using its segmentation results on a video of an Adipic Acid crystallization experiment at each step of the method. Nevertheless, the results on the Adipic Acid crystallization video are presented solely to illustrate the image analysis method. Therefore, we do not provide any physico-chemical interpretation of the results; instead, we discuss them from an image analysis perspective.

2 Material and methods

2.1 Experimental device

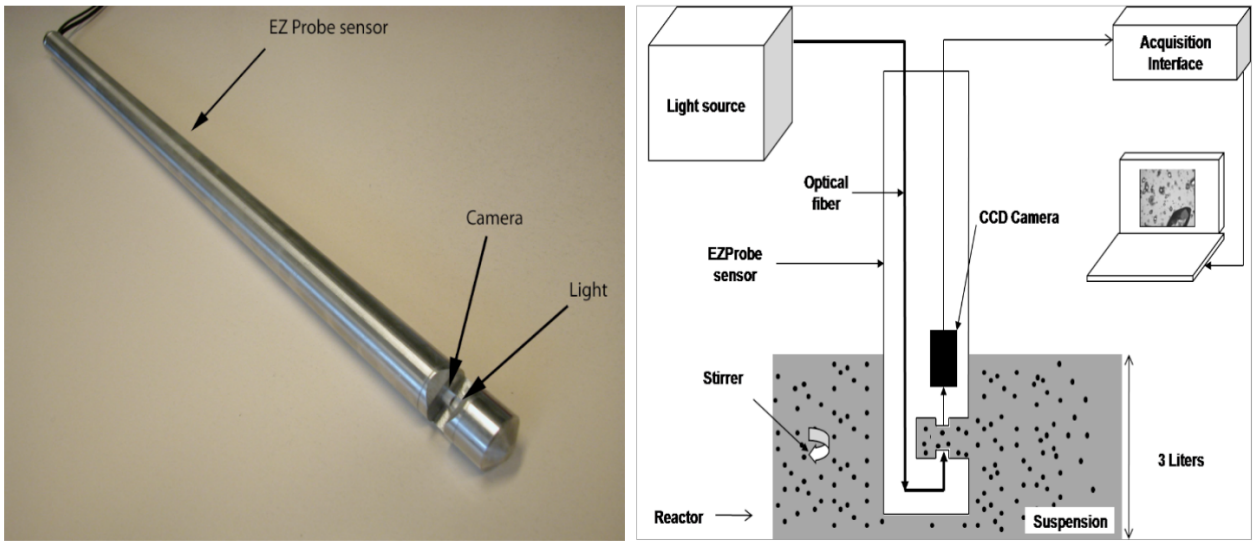

Fig 1 Diagram of the experimental device (right) and representation of the EZ probe sensor (left).

Batch crystallization experiments were conducted in a reactor equipped with a stirrer. *In-situ* sensors, including an acoustic emission sensor and an image sensor known as the EZ probe, were deployed. The EZ probe was developed by a university laboratory, the LAGEPP (Laboratoire d'Automatique, de Génie des Procédés et de Génie Pharmaceutique, UCBL Lyon1 – CNRS) specifically for the monitoring of crystallization processes, more details can be found in.[31] The EZ probe has a diameter of $25\,mm$ and a length of approximately $300\,mm$, it comprises a fiber-optic bundle-supported light source that illuminates a CCD camera using transmitted light. The camera

captures 25 images per second with a spatial resolution of $4\,\mu m^2$ per square pixel. This probe records real-time footage of a small volume ($1.3\,mm \times 1\,mm \times 1\,mm$) of the suspension. The analysed field covers $1.3\,mm \times 1\,mm$ for 640×480 pixel images, with a $1\,mm$ air gap within the probe.

2.2 Observation of the data

In order to address the issue, crystallization experiments were conducted for various types of products under different experimental conditions. Images acquired during these experiments are depicted in Figure 2, where we can observe a wide diversity in crystal morphology. Indeed, various crystal shapes emerge, including needles, blocks, and polyhedra. However, apart from the convexity of the crystals, it appears challenging to establish a general morphological model independent of the product and experimental conditions. Moreover, crystal segmentation for such images seems quite complex for various reasons: blurry particles, overlaping particles, and sometimes shiny or transparent crystals.

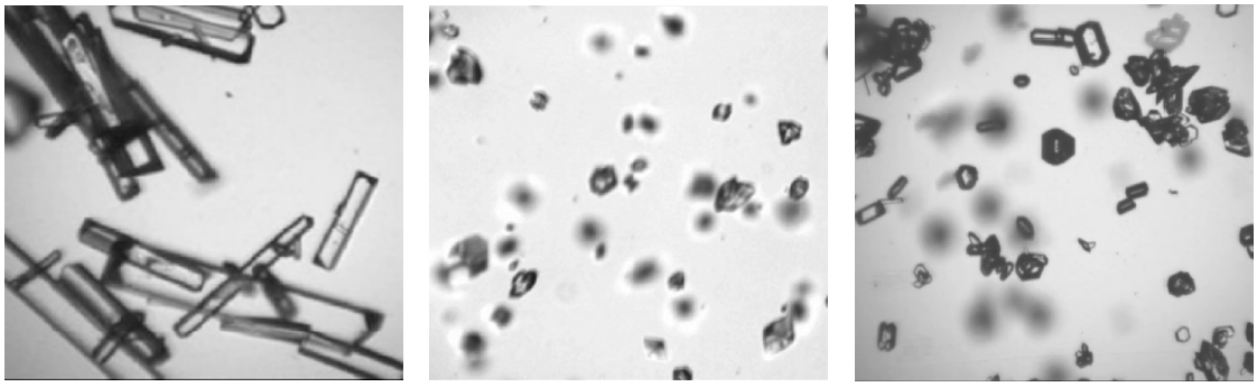

Fig 2 EZ probe acquisitions of different types of crystals (from left to right): Ammonium Oxalate, Citric Acid and Adipic Acid.

Observation of the videos reveals that the probe becomes clogged during the crystallization

process, as shown in Figure 3. Throughout the video, as it passes through the air gap, crystals occasionally agglomerate within the gap and with each other. These aggregates then persist throughout the rest of the video, with some aggregates detaching at times. Consequently, the probe's air gap gradually clogs until it is completely obstructed. At this stage, no crystals are visible, and only a large mass of crystals adhered to the air gap remains visible. While favorable experimental conditions, such as strong agitation, may delay this phenomenon, it ultimately occurs. Nevertheless, from the beginning of crystallization until a certain level of air gap clogging is reached, the video allows us to visualize a portion of the crystals present in the reactor *in-situ*.

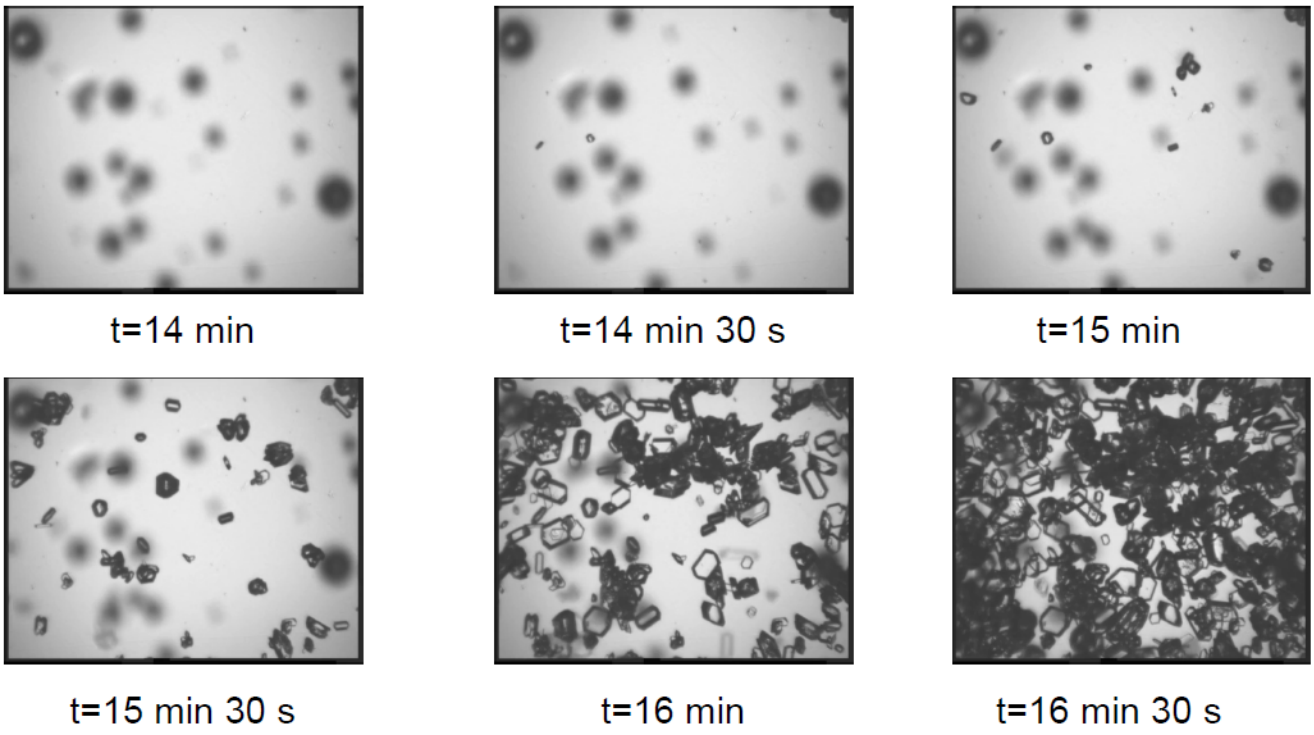

Fig 3 Images of the air gap clogging at various time points from a 45-minute video of the crystallization of Adipic Acid. Out of the 45-minute video, only the first 16 minutes are usable, as the air gap becomes excessively clogged beyond that point.

In order to control and monitor the crystallisation process, there are several compelling reasons to analyse the videos captured by the EZ Probe. The main objective is to acquire quantitative data

concerning the number, dimensions and morphology of the crystals/aggregates in the reactor (particle size distribution) at each time. Indeed, there are few *in-situ* alternatives to image analysis for obtaining such information.[8,17] Additionally, there are specific challenges associated with image analysis. The employed tools must exhibit both robustness and versatility to handle diverse crystal types with varying morphologies. Furthermore, these tools must be capable of handling images with fluctuating crystal densities, particularly in scenarios of high density due to probe fouling.

3 Dynamic segmentation of crystals aggregate

Below, we introduce the method developed for segmenting crystallization videos captured by the EZ Probe. To begin, we'll explain the preprocessing steps applied to the images to achieve an initial image binarization. Subsequently, we'll use the dynamic phenomena observed in the videos to refine the image binarization process and to differentiate between crystals adhering to the gap and those passing through the probe.

3.1 First detection of the cristals phase

Firstly, our method consists of a simple binarisation of each frame of the video. To do this, we tested several existing methods for different types of crystal. It appeared that the application of global thresholding using Otsu's method, after a few adjustments to the contrast and background effect, gave the best results.

Let $I^{(t)}$ be the frame at time index t (To streamline notations, indices will be omitted when no confusion arises). Each image is then considered as a matrix with dimensions of 576×720 with values in the range $[0, 1]$. Some preprocessing operations are performed before binarization; the

black border edge of the image is cropped, then an adjustment to the background is applied and finally the contrast is adjusted.

The first step is straightforward, with the user specifying the cropping window of interest. For our examples, this window is $[10, 6, 700, 557]$, which results in an image of size 558×701 as shown in the illustrations.

During the initial minutes of the process, no crystals have formed in the reactor, though impurities from the reactor or air gap may be visible in the images. These initial images essentially represent the background and will be used for background image extraction. Particles appear on the screen as darkened areas, allowing us to treat the background as the image with the highest gray levels (per pixel) across the video frames. We achieve this by computing the background image as the maximum gray levels over a specific time period and applying Gaussian filtering. Specifically, we execute the following operation:

$$\forall ij,\ F_{ij} = max\{I_{ij}^{(t)}, 0 \leq t \leq T\}$$

$$F \leftarrow imgaussfilt(F, ...),$$

Where T denotes the number of frames used for background calculation. While all video frames can be employed, the initial one thousand frames yield satisfactory results. Subsequently, a Gaussian filter is applied to smooth the background and enhance calculation robustness, reducing sensitivity to the Max operator. The results of these background calculations for Adipic Acid crystals are presented in Figure 4.

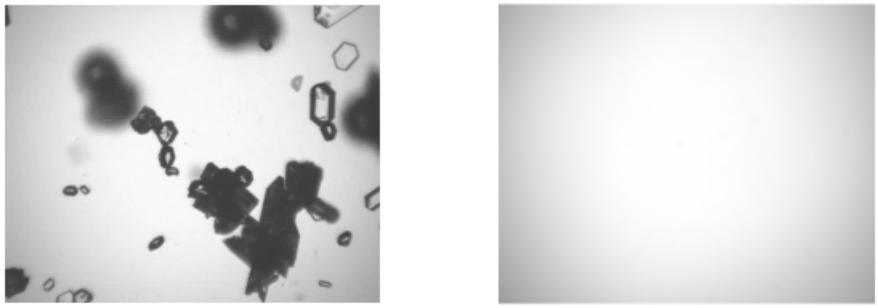

Fig 4 An original image from a video of Adipic Acid crystalization and the background calculated from the first thousand frames.

The background F is non-uniform, and it seems that the gray level of a crystal varies with its position. Therefore, it is necessary to remove this background effect before binarization. To achieve this, we chose a multiplicative transformation, which aligns better with the optical properties of crystals than a simple subtraction. Specifically, we apply the following transformation:

$$I_{ij} \leftarrow (F_{ij})^{-1} I_{ij}. \tag{1}$$

Following this transformation, a non-linear contrast adjustment (gamma correction) is performed, the results of these transformations are presented in Figure 5.

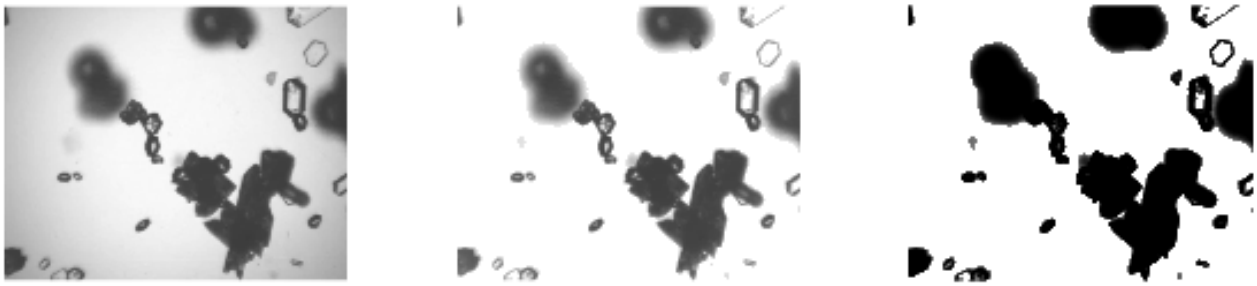

Fig 5 Original image on the left, background-adjusted image in the center, and contrast-adjusted image on the right.

These pre-processing steps effectively enhance crystal detection through binarization, creating

ample contrast between crystal edges and the new background for easier identification. Binarization is performed using the Otsu method, as shown in Figure 6. While it accurately detects crystal edges, distinguishing the interiors of crystals remains challenging. While it's possible to perform filling operations on the interiors of connected components, distinguishing holes in aggregates from the interiors of crystals is a complex task. Therefore, it's more sensible to use video dynamics to differentiate beforehand between aggregates adhering to the air gap and moving aggregates.

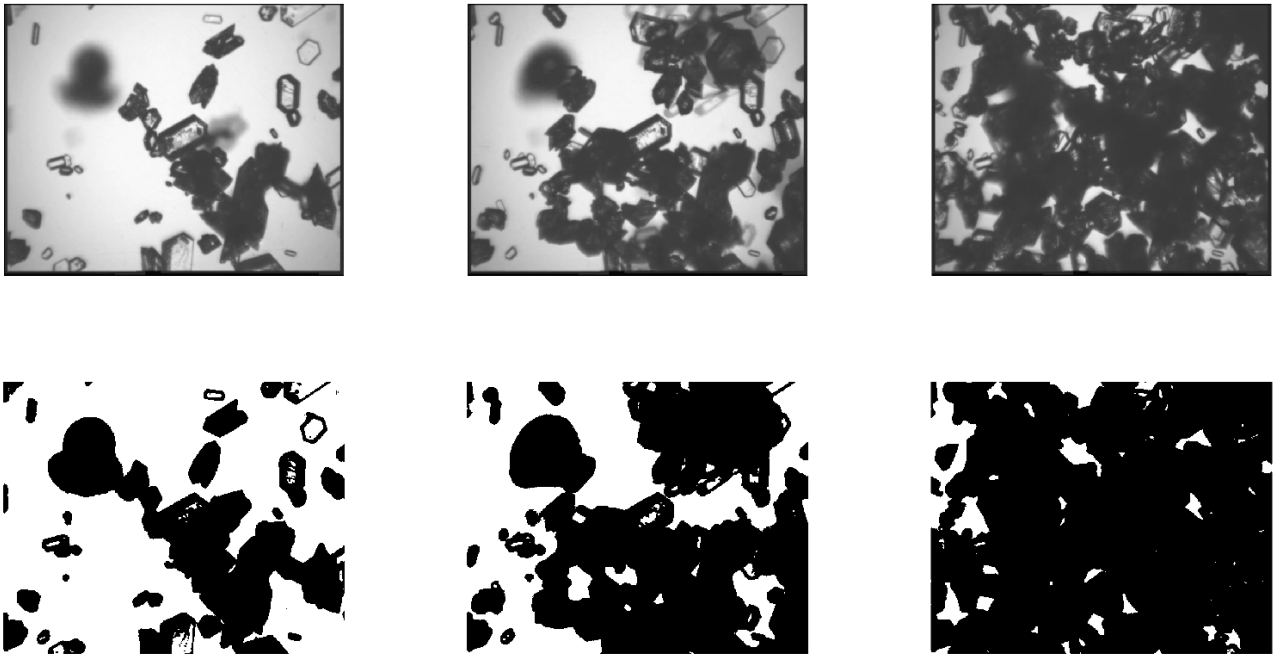

Fig 6 Images of Adipic Acid crystals and their binarizations.

3.2 Splitting of the glued and moving aggregate

Upon reviewing the videos, we observe the presence of two distinct dynamics. On one hand, there are aggregates that adhere to the air gap and move slowly in comparison to the probe's sampling frequency. On the other hand, there are mobile aggregates that move much more rapidly, as depicted in Figure 7. This phenomenon will enable us to differentiate between aggregates fixed

to the air gap and those in motion Let's note, $B^{(t)}$ the binarisation of $I^{(t)}$ at time t and $C^{(t)}$ the

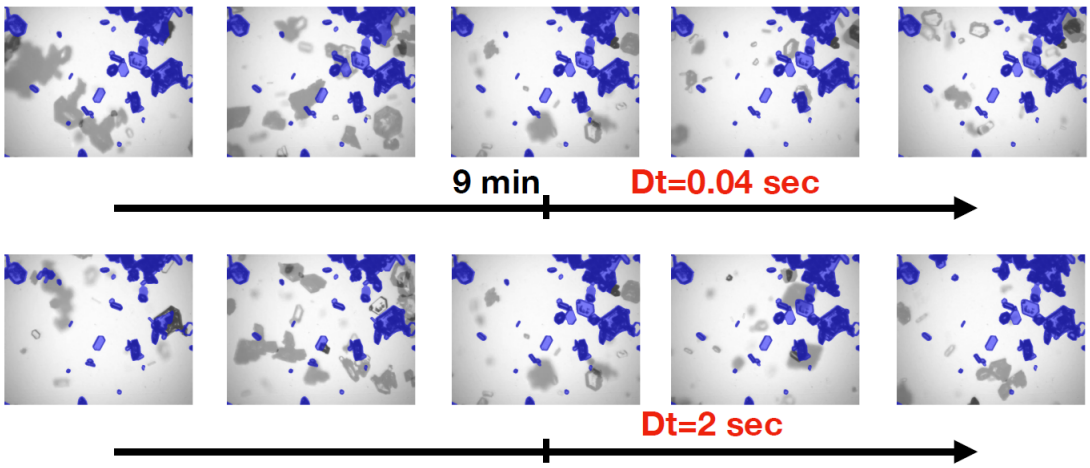

Fig 7 Two image sequences extracted from a video of Adipic Acid crystallization. These sequences are centered at a time $t_0 = 9\,min$ and have respective increments of $2\,s$ and $0.04\,s$ seconds (the camera's sampling frequency is $0.04\,s$). It is noteworthy that the portion of aggregates adhering to the air gap (highlighted in blue) evolves at a much slower rate compared to the rest of the aggregates.

binary image corresponding to the glued part (aggregates glued to the air gap) (the superscript $...^{(t)}$ will be omitted when there is no ambiguity). So, by analysing the binary video and using a temporal filter, it is possible to distinguish the glued part $C^{(t)}$. If we consider a time interval centred at t, the clipped part $C^{(t)}$ corresponds to the intersection of the images in the interval. To be precise, for an instant t_0 the $2n+1$ binary images of the discrete interval $\{t_0 - n\Delta t, \cdots t_0, \cdots t_0 - n\Delta t\}$ are considered, a pixel will then belong to the image $C^{(t_0)}$ if it belongs to at least $\alpha\%$ of the images in the interval. This temporal filter provides a robust estimate of the intersection of the $2n+1$ binary images. In practice, we have chosen: $n = 10$, $\alpha = 0.8$ and an increment $\Delta t = 0.04\,s$ corresponding to the sampling frequency of our videos. Esspecialy we have:

$$[C^{(t_0)}]_{ij} := [(\sum_{t_0-n}^{t_0+n} B^{(t)}) > \alpha(2n+1)]_{ij},\ \forall ij \tag{2}$$

The binary image $C^{(t)}$ corresponding to the aggregates glued to the air gap, is subsequently

improved through a ”cleaning” procedure. This procedure employs standard morphological operations (opening, closing using a ball), as well as a hole-filling operation for connected components.

Next, the remaining aggregates, denoted as $R^{(t)} = B^{(t)} \setminus C^{(t)}$, also undergo the same cleaning procedure. Finally, the binary image corresponding to all aggregates in $B^{(t)}$ (regardless of whether they are adhered to the air gap) is obtained by simple uniting $B^{(t)} \leftarrow R^{(t)} \cup C^{(t)}$. This approach, involving a multi-stage segmentation refinement process (cleaning $C^{(t)}$, then $R^{(t)}$, and finally uniting them), prevents the filling of holes that do not correspond to the interiors of crystals, which could otherwise result from the overlap of moving aggregates with those glued to the air gap.

In the end, each image is segmented into two parts: the binary image corresponding to all aggregates, denoted as $B^{(t)}$, and the image $C^{(t)}$ representing the aggregates glued to the air gap. For the analysis of moving aggregates, not all related components of $B^{(t)}$ can be considered. This is because some related components intersect the image's edge and/or the glued part $C^{(t)}$. Therefore, for the study of moving aggregates, we can consider that we have a restricted spatial support that evolves over time $W \backslash C^{(t)}$ (where W designates the rectangular observation window). Thus, we will construct the image $D^{(t)}$ corresponding to the completely detected moving aggregates as the set of connected components of $B^{(t)}$ strictly included in $W \backslash C^{(t)}$ (i.e., those which intersect neither the edge of the image nor the glued part $C^{(t)}$).

Finally, at each instant of the video, three binary images will be stored: $B^{(t)}$ corresponding to all aggregates on the screen, $C^{(t)}$ corresponding to the aggregates glued to the air gap, and $D^{(t)}$ representing the aggregates in full visible motion. These three binary images will then be saved in

each of the channels of an RGB image. The outcome is an RGB video that segments the original video.

3.3 Segmentation results and discussion

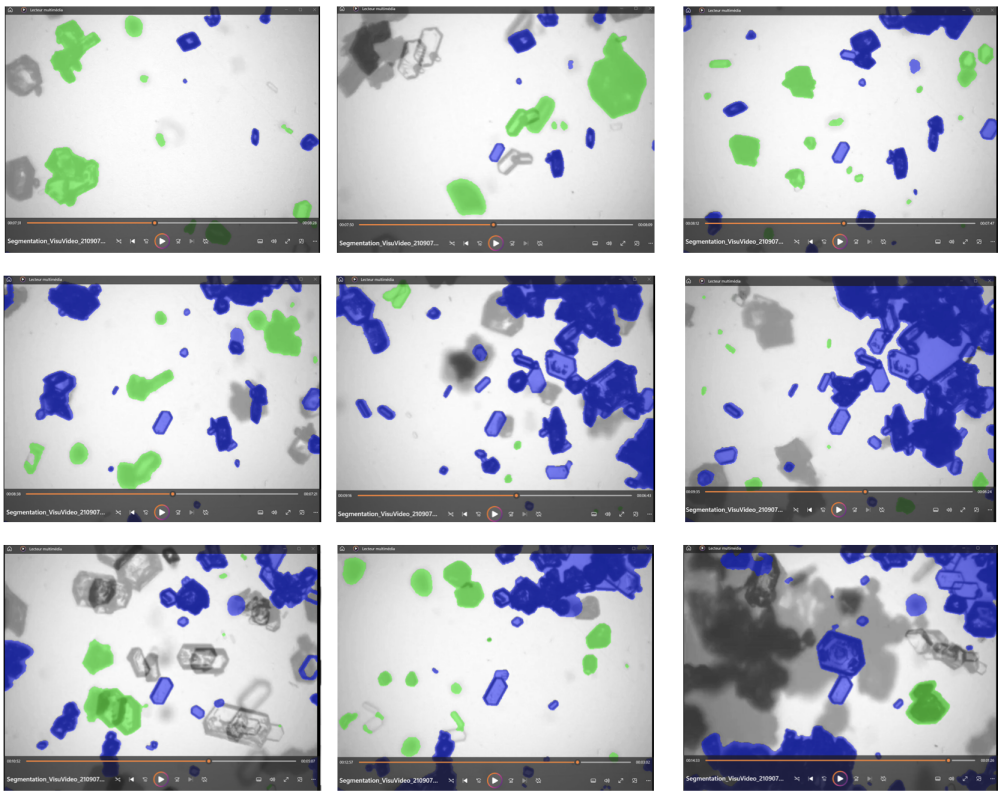

Fig 8 Images from a segmented video, depicting only parts $C^{(t)}$ and $D^{(t)}$. In blue, the glued aggregates, and in green, the fully detected moving aggregates.

We have implemented and tested this method on various crystallization videos. Since we lacked a segmentation reference, the assessment of segmentation quality relied on visual observation. The results, as shown in Figure 8, are quite compelling. We've achieved a satisfactory differentiation between the glued and mobile aggregates, and the number of detected moving aggregates is sufficiently large for statistical representation.

However, the obstruction of the air gap imposes limitations on the study for several reasons. Firstly, beyond a certain level of probe clogging, the segmentation of the glued part becomes less

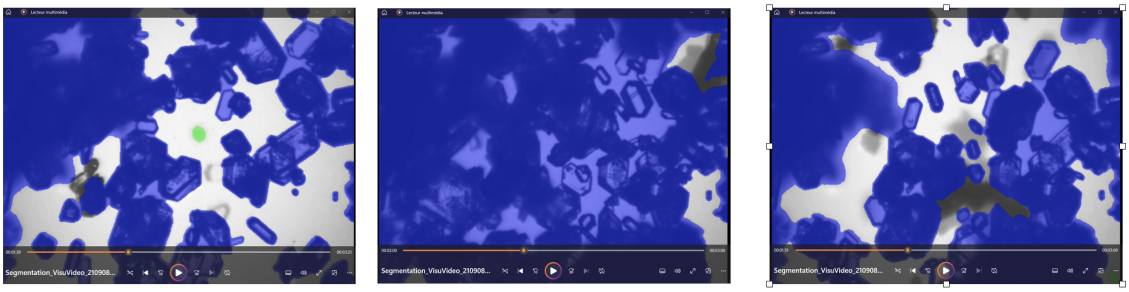

Fig 9 Critical cases with excessive air gap clogging result in poor segmentation of the glued part and a spatial support too constrained for accurate moving aggregate detection.

effective, resulting in erroneous hole-filling in connected components. Secondly, the available spatial support for detection, $W \backslash C^{(t)}$, becomes too limited, resulting in a reduced number of detections and the inability to detect large aggregates, as shown in Figure 9. Thirdly, the fouling of the probe and the evolving nature of the spatial support introduce an observation bias. This is why we will use a Bayesian bias corrector introduced later. In cases where fouling is particularly severe, as illustrated in the critical scenarios presented in Figure 9, the spatial support for aggregate detection becomes too limited, rendering observation impossible. In practice, we apply a threshold on the surface of the spatial support, limiting our analysis to periods when aggregates are detectable.

4 Quantitative analysis

The glued part $C^{(t)}$ and the detected part $D^{(t)}$ yield distinct insights into the crystallization process. In the glued part, aggregates can be tracked across consecutive video frames, facilitating the observation and quantification of their growth. The analysis of $C^{(t)}$ provides the temporal evolution of quantitative characteristics (e.g., area, diameter, equivalent diameter) for each air gap-adhered aggregate, allowing us to infer their growth kinetics. It's worth noting, however, that due to hydrodynamic factors, the kinetics of gap-adhered crystals may not necessarily reflect those within the reactor.

Analysis of the detected part $D^{(t)}$ provides abundant quantitative insights into the process. The evolution of the number of detected aggregates (connected components) detected over time highlights the key stages of crystallisation. Additionally, all geometric and morphological characteristics of these aggregates are readily accessible at any moment, allowing for instantaneous granulometric distributions. It's important to note that the detection method employed with the restricted spatial support $W \backslash C^{(t)}$ introduces a bias. Larger aggregates have a lower probability of being entirely visible (strictly within $W \backslash C^{(t)}$) compared to smaller ones. Furthermore, this bias intensifies as the air gap gets clogged (with increasing $C^{(t)}$). However, implementing bias correction accounting for spatial support can be used.

4.1 Biais correction for the moving aggregates

The detection of moving aggregates $D^{(t)}$ is performed on a dynamic spatial support, $W \backslash C^{(t)}$, which evolves over time, gradually decreasing, introducing bias. However, employing Bayesian bias correction under reasonable probabilistic assumptions is feasible.

Consider the original observation window W and assume an aggregate X is a random set wich appears within the window with uniform position, independent of its dimensions. In other words, the center x of X is considered to have a uniform distribution across W. Then, the conditional probability of this aggregate X being visible (i.e., $X \subset D^{(t)}$) knowing it takes a values Y can be directly expressed.

Indeed, X is visible if and only if its center belong to the eroded spatial support $x \in (W \backslash C^{(t)}) \ominus$

X, thus according to the uniform position of X:

$$\mathbb{P}(X \text{ is visible} \mid X = Y) = \frac{A((W \backslash C^{(t)}) \ominus Y)}{A(W)}. \tag{3}$$

Subsequently, these probabilities calculated for all observed aggregates are employed to weight the histograms of their geometric characteristics. In practical terms, the objective is to enhance the representativeness of observations with a lower likelihood of visibility. In essence, the probability of an aggregate's appearance is deduced from both its observation and the likelihood of it being visible.

More specifically, let X represent the random set associated with the aggregate, and consider a family of n observed aggregates denoted as $\{X_1, \ldots, X_n\}$. We define the weight of the observation X_i at time t_i as:

$$\omega_i = A((W \backslash C^{(t_i)}) \ominus X_i), \tag{4}$$

where t_i denotes the instant of the observation. The application of Bayes'rule yields:

$$\mathbb{P}(X = X_i) = \sum_{k=1}^{n} \frac{\omega_k}{n\omega_i} \mathbb{P}(X = X_k), \tag{5}$$

wich is solved as:

$$\mathbb{P}(X = X_i) = (\sum_{k=1}^{n} \frac{\omega_i}{\omega_k})^{-1}. \tag{6}$$

The computation of the weight involves morphological operations (erosion), which can be

costly for specific shapes of X_i. Consequently, to improve computational efficiency, it is more judicious to use a ball with an equivalent diameter of X_i (e.g., the equivalent diameter of the convex hull). Such simplification for the weight computation has a pertinent theoretical foundation according to the generalized Steiner formula for erosion[32] if the random aggregate is assumed to be isotropic.[33]

The computation of the discrete distribution among the observed aggregates provides a direct distribution of various geometric and morphological characteristics relevant to practitioners, including, area, perimeter, equivalent diameters, and Feret's diameter. This allows, among other things, the calculation of the particle size distribution of aggregates for various size-related characteristics. Due to the non-convex nature of these aggregates, it's advisable to prioritize measurements that are unaffected by convexity, such as maximal Feret diameter or other characteristics associated with the convex hull of the aggregates.

Practically, to enhance the data's representativeness, the aggregate distribution at time t_0 is derived from the aggregates detected within a time window $[t_0 - a; t_0 + a]$ centered at t_0. We selected a time window with a 5-second amplitude. The evolving of maximal Feret diameter distributions for a video of Adipic Acid crystallization are presented in Figure 10. We can observe, firstly, that the particle size distribution becomes increasingly scattered over time. As the reaction progresses, larger aggregates are detected. Secondly, the total number of detections over time exhibits a characteristic phase of exponential growth, indicative of the reaction kinetics.

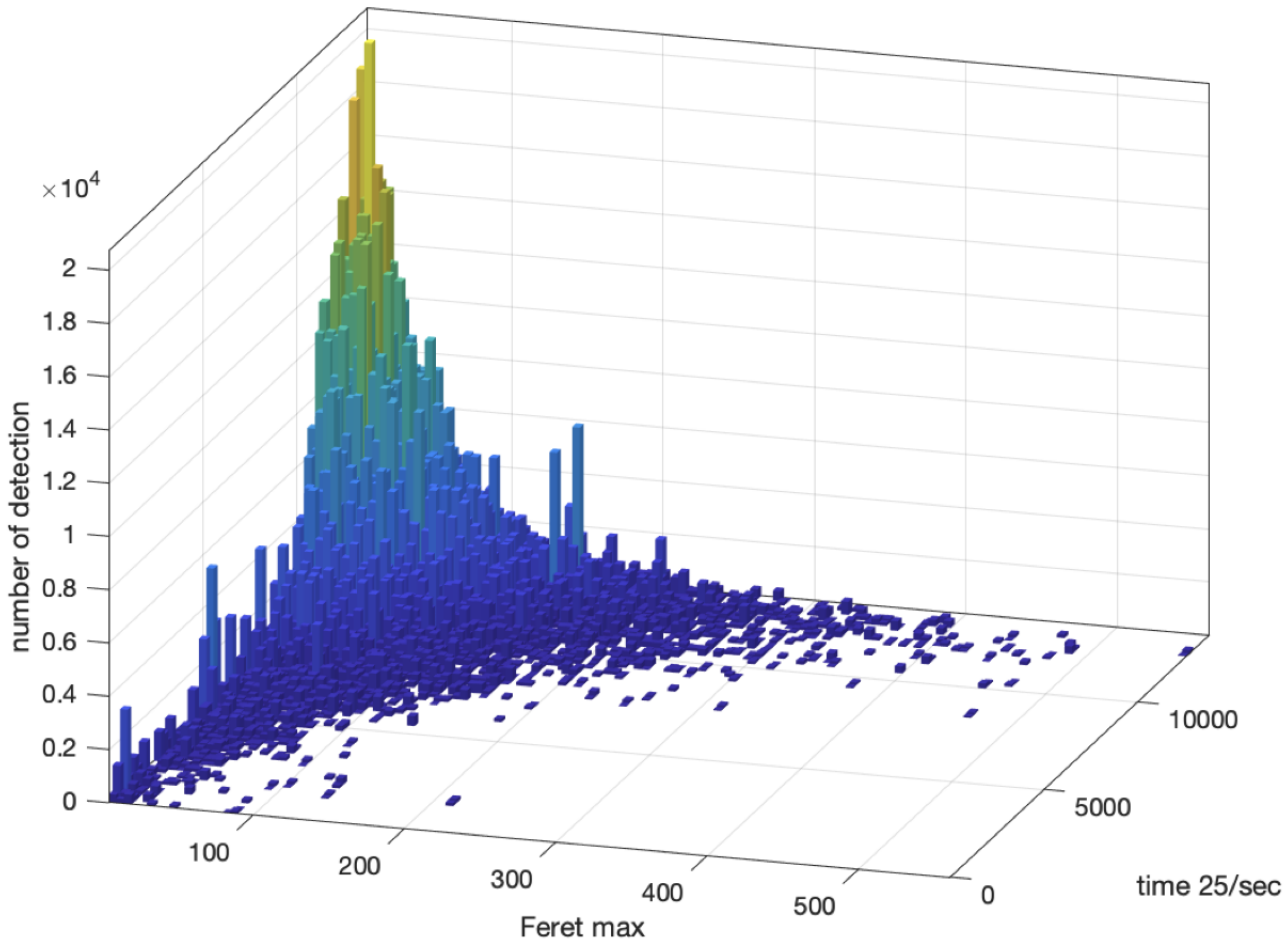

Fig 10 Distribution histograms of the maximum Feret diameter over time, for a video of Adipic Acid crystallization. The Feret's diameters unit is in pixels length (according to our spatial resolution 1 pixel $= 2\mu m$).

4.2 Analysis of the glued aggregates

The aggregates of the glued part, $C^{(t)}$ can be tracked across numerous frames, enabling clear observation of their growth. By examining these aggregates in segmented crystallization videos, their growth becomes readily visible (see video in attachment). Consequently, the dynamic analysis of the connected components of $C^{(t)}$ (i.e., the aggregates adhering to the air gap) reveals insights into the kinetics of crystal growth. However, several observations need to be made to quantify this growth.

The connected components of the glued part, that is, the aggregates attached to the air gap, display

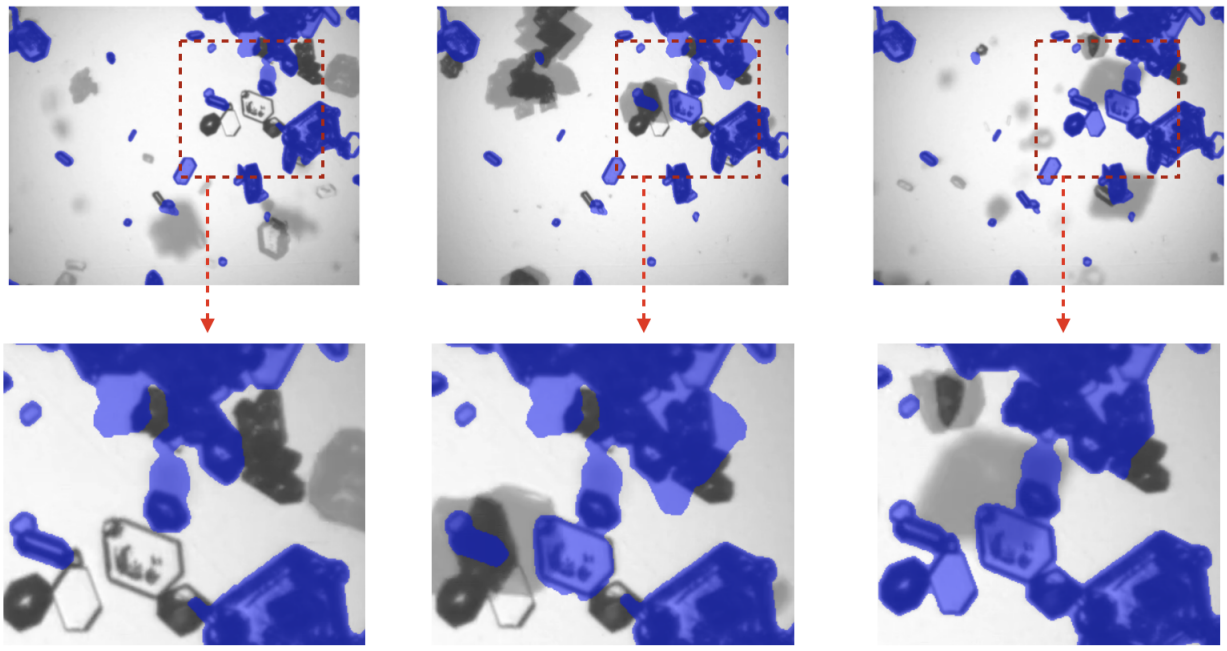

Fig 11 Example of the evolution of the glued part at three time points from a video of Adipic Acid crystallization.

various growth patterns, as illustrated in Figure 11. On one hand, they undergo continuous intrinsic growth due to the crystals' own development. On the other hand, they experience intermittent growth due to the arrival of new aggregates on the air gap and/or the merging of connected components. Additionally, there are instances where an aggregate detaches from the air gap. These diverse forms of evolution consequently alter the topological structure of $C^{(t)}$.

In order to quantify the growth of aggregates adhered to the air gap, it is essential to consider the evolution of the topological structure of $C^{(t)}$. Rules for distinguishing between the various types of component growth must be established. To achieve this, we employ connected component trees.[34,35] This tool allows us to summarize the topological evolution of the structure over time, capturing phenomena such as component fusion and the appearance of new aggregates. This approach reveals the different modes of growth of connected components, as depicted in Figure 12.

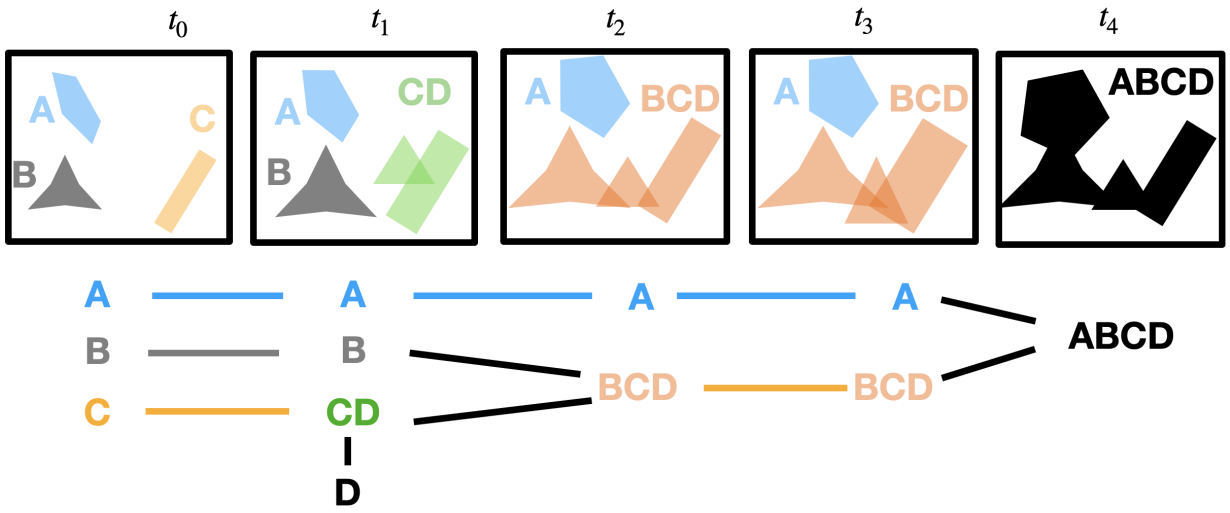

Fig 12 llustration of the aggregate tracking rule and the corresponding connected component tree. Here, three aggregates are tracked: aggregate (A) is tracked during the period $[t_0, t_3]$, aggregate (B) during $[t_0, t_1]$, and aggregate (BCD) during $[t_2, t_3]$.

The tracking of an aggregate between two images is carried out using a morphological distance: a connected component A_t present in image t is tracked at time $t+1$ if and only if A_{t+1} has a shape that is sufficiently close to A_t. Specifically, the rule considered is as follows: Component A_t persists at time $t+1$ if and only if:

$$A_{t+1} \subset A_t \oplus B(0, r), \tag{7}$$

where r is a small chosen value that serves as a prior bound for $\frac{\Delta d(A)}{\Delta t}$, the discrete derivative of the diameter of A.In practice, choosing the value of r is straightforward, as the instantaneous continuous growth of an aggregate between two successive images is very small compared to the size of new aggregates that would adhere to the air gap. In our case, we chose a ball with a radius of 5 pixels.

Finally, applying the aforementioned tracking rule, the extraction of tree branches without

fusions allows the identification of periods during which a connected component can be tracked, as shown in Figure 12. For each tracked aggregate, the evolution of its diameter is obtained over the entire tracking period. This provides, among other things, information about the kinetics of crystal growth. The evolution of the equivalent diameter of aggregates adhering to the air gap during Adipic Acid crystallization is depicted in Figure 13. These results reveal the presence of a temporally localized growth phase with a distinctive profile. Such data would enable experts to adjust parameters of physico-chemical models of crystal growth kinetics.

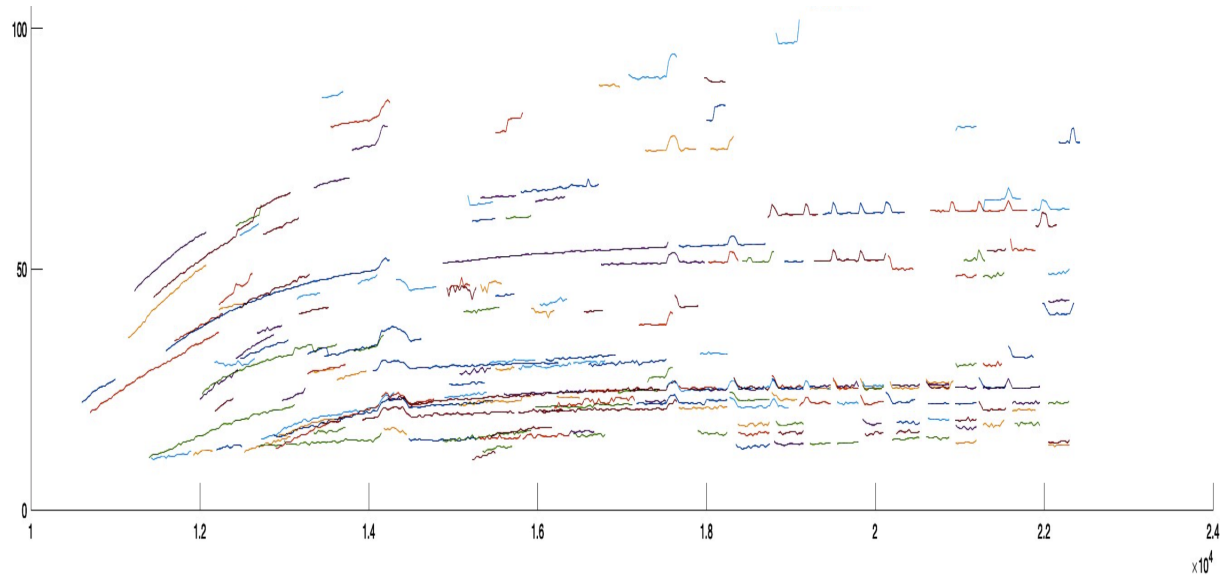

Fig 13 Evolution of the diameter of the different aggregates adhered to the gap followed during their respective periods (each curve corresponds to the tracking of an aggregate). The diameters unit is in pixels length (according to our spatial resolution 1 pixel $= 2\mu m$).

5 Conclusion and prospect

5.1 Conclusion

The proposed method effectively addresses our industrial challenge by enabling the quantitative analysis of crystal aggregates from data provided by our acquisition system, regardless of the considered crystal morphologies. This is a semi-supervised approach where the operator configures

the segmentation parameters for video analysis, observes the segmented video, and then selects a relevant period for quantitative characterization of the aggregates. This approach leverages the dynamics of the acquired videos and the phenomenon of probe fouling to extract quantitative information about the crystallization process.

In particular, the analysis of the detected part, denoted as $D^{(t)}$, reveals a wealth of quantitative information about the process. It provides access to the particle size distribution of the aggregates in the reactor over time and highlights the key stages of crystallization. On the other hand, the analysis of the glued part, denoted as $C^{(t)}$, allows us to track the evolution of aggregates adhered to the gap, thereby deducing the growth kinetics of these crystals. However, it is important to note that, due to hydrodynamic reasons, the kinetics of glued crystals may not necessarily reflect those of the crystals present in the reactor.

This method has several limitations. Firstly, beyond a certain degree of probe fouling, the segmentation becomes less relevant, thereby hindering quantitative analysis. Furthermore, the proposed characterization is limited to the scale of the aggregates. Lastly, it is essential to bear in mind that the characterizations and quantifications pertain to the 2D projections of the aggregates. Therefore, caution should be exercised in their interpretation, particularly because these aggregates are not necessarily convex.[23,36]

5.2 Prospects

From an application perspective, various opportunities arise based on the practical objectives envisioned, as the segmentation method provides direct access to the projections of aggregates. However, from the standpoint of our study, this method's primary limitations lie in its restriction to the aggregate scale and the confined characterization to 2D projections. To address these limitations, it would be interesting to achieve a finer 3D characterization of the process, focusing on the scale of individual crystals.

For this purpose, accessing the aggregate projections provided by the proposed segmentation, combined with stochastic geometric models of aggregates, presents a promising perspective. Recent work on a similar issue has demonstrated encouraging results.[37] The underlying idea involves constructing a realistic 3D model of crystal aggregates, which would subsequently be characterized by the numerous aggregate projections available through the segmentation method. Ultimately, this would allow for the direct characterization of the 3D geometry distribution of individual crystals. It is worth noting that this approach necessitates restrictive assumptions about crystal morphology, yet it remains a promising prospect for specific targeted applications.

Code and data availability

The data that support the findings of this article are not publicly available due to our confidentiality agreements with our partners.

Author biographies

Saïd Rahmani is a post-doctoral researcher at MINES Saint-Etienne, France. His research interests include stochastic geometry, spatial statistics, mathematical morphology, pattern

recognition and image analysis.

Roger de Souza Lima is a chemical engineer in the Research & Development team at INEVO, France. He received a master's degree in Chemical Engineering from Ecole Nationale Supérieure en Génie des Technologies Industrielles (ENSGTI) in Pau, France, and a PhD in Chemical Engineering from IMT Mines Albi in Albi, France. His field of work involves developing models based on multi-phase industrial unit operations.

Eric Serris is a research engineer PhD in Mines Saint-Etienne for more than twenty years. His research topics are powder technology and processing and acoustic emission for chemical engineering.

Ana Cameirão is a Full Professor at MINES Saint-Etienne, France. Her research interests include industrial crystallization, crystallization under flow, cristal growth, agglomeration, inline measurements and population balance.

Johan DEBAYLE is a Full Professor at MINES Saint-Etienne, France. His research interests include image analysis, mathematical morphology, pattern recognition and stochastic geometry.

References

1 R. de Souza Lima, A. Cameirão, and E. Serris, "Use of acoustic emission to monitor adipic acid crystallization," in European Conference on Acoustic Emission Testing (EWGAE35 & ICAE10), (2023-01), NDT. net (2022).

2 X. Wang, Y. Huang, and T. M. Michelitsch, "Acoustic emission detection of crystallization

in two forms: monohydrate and anhydrous citric acid," Pharmaceutical Development and Technology **24**(4), 419–426 (2019).

3 N. Gherras, E. Serris, and G. Févotte, "Monitoring industrial pharmaceutical crystallization processes using acoustic emission in pure and impure media," International Journal of pharmaceutics **439**(1-2), 109–119 (2012).

4 Y. Zheng, X. Wang, and Z. Wu, "Machine learning modeling and predictive control of the batch crystallization process," Industrial & Engineering Chemistry Research **61**(16), 5578–5592 (2022).

5 Z. K. Nagy, M. Fujiwara, R. D. Braatz, et al., "Monitoring and advanced control of crystallization processes," Handbook of Industrial Crystallization **3** (2019).

6 Y. Zhou, R. Srinivasan, and S. Lakshminarayanan, "Critical evaluation of image processing approaches for real-time crystal size measurements," Computers and Chemical Engineering **33**(5), 1022–1035 (2009).

7 B. Presles, J. Debayle, and J. C. Pinoli, "A novel projective stereological image analysis method to estimate particle size and shape distributions," in 10th IEEE/SPIE International Conference on Quality Control by Artificial Vision (QCAV), (Fukuoka, Japan) (2013).

8 B. Presles, Caractérisation géométrique et morphométrique 3-D par analyse d'image 2-D de distributions dynamiques de particules convexes anisotropes. Application aux processus de cristallisation. PhD thesis, Ecole Nationale Supérieure des Mines de Saint-Etienne (2011).

9 Y. Huo, T. Liu, H. Liu, et al., "In-situ crystal morphology identification using imaging analysis with application to the L-glutamic acid crystallization," Chemical Engineering Science **148**, 126–139 (2016).

10 X. Wang, J. Calderon De Anda, and K. Roberts, "Real-time measurement of the growth rates of individual crystal facets using imaging and image analysis: a feasibility study on needle-shaped crystals of l-glutamic acid," Chemical Engineering Research and Design **85**(7), 921–927 (2007).

11 O. Ahmad, J. Debayle, N. Gherras, et al., "Recognizing overlapped particles during a crystallization process from in situ video images for measuring their size distributions," in 10th SPIE International Conference on Quality Control by Artificial Vision (QCAV), (Saint-Etienne, France) (2011).

12 O. Ahmad, J. Debayle, N. Gherras, et al., "Quantification of overlapping polygonal-shaped particles based on a new segmentation method of in situ images during crystallization," Journal of Electronic Imaging **21**(2), 1–12 (2012).

13 B. Presles, J. Debayle, A. Rivoire, et al., "Monitoring the particle size distribution using image analysis during batch crystallization processes," in 9th IEEE/SPIE International Conference on Quality Control by Artificial Vision (QCAV), (Wels, Austria) (2009).

14 B. Presles, J. Debayle, G. Fevotte, et al., "A novel image analysis method for in-situ monitoring the particle size distribution of batch crystallization processes," Journal of Electronic Imaging **19**(3), 1–7 (2010). Special Section on Quality Control by Artificial Vision.

15 S. Outal, Quantification par analyse d'images de la granulométrie des roches fragmentées: amélioration de l'extraction morphologique des surfaces, amélioration de la reconstruction stéréologique. PhD thesis, École Nationale Supérieure des Mines de Paris (2006).

16 J. Serra and P. Soille, Mathematical morphology and its applications to image processing, vol. 2, Springer Science & Business Media (2012).

17 O. S. Ahmad, J. Debayle, and J.-C. Pinoli, "A geometric-based method for recognizing overlapping polygonal-shaped and semi-transparent particles in gray tone images," Pattern Recognition Letters **32**(15), 2068–2079 (2011).

18 S. Schorsch, D. Ochsenbein, T. Vetter, et al., "High accuracy online measurement of multi-dimensional particle size distributions during crystallization," Chemical Engineering Science **105**, 155–168 (2014).

19 J. Calderon De Anda, X. Wang, and K. Roberts, "Multi-scale segmentation image analysis for the in-process monitoring of particle shape with batch crystallisers," Chemical Engineering Science **60**(4), 1053–1065 (2005).

20 S. Rahmani, R. De Souza Lima, A. Cameirao, et al., "Particles detection in a 2d-image of overlapping crystals based on community detection," in 13th European Congress for Stereology and Image Analysis (ECSIA), (Saint-Etienne, France) (2021).

21 Y. Huo, D. Guan, and X. Li, "In situ measurement method based on edge detection and superpixel for crystallization imaging at high-solid concentrations," Crystals **12**(5), 730 (2022).

22 J. Wan, C. Y. Ma, and X. Z. Wang, "A method for analyzing on-line video images of crystallization at high-solid concentrations," Particuology **6**(1), 9–15 (2008).

23 E. E. Underwood, "The stereology of projected images," Journal of microscopy **95**(1), 25–44 (1972).

24 L. Theodon, T. Eremina, K. Dia, et al., "Estimating the parameters of a stochastic geometrical model for multiphase flow images using local measures," Image Analysis and Stereology (40), 115–à (2021).

25 S. Rahmani, J.-C. Pinoli, and J. Debayle, "Geometrical stochastic modeling and characterization of 2-d crystal population," Acta Stereologica (2015).

26 M. de Langlard, La géométrie aléatoire pour la caractérisation de populations denses de particules: application aux écoulements diphasiques. PhD thesis, Université de Lyon (2019).

27 T. Eremina, J. Debayle, F. Gruy, et al., "Local measures distribution for the estimation of the elongation ratio of the typical grain in homogeneous boolean models," Image Analysis & Stereology **40**(2), 95–103 (2021).

28 K. He, G. Gkioxari, P. Dollár, et al., "Mask r-cnn," in Proceedings of the IEEE international conference on computer vision, 2961–2969 (2017).

29 F. C. Walter, S. Damrich, and F. A. Hamprecht, "Multistar: Instance segmentation of overlapping objects with star-convex polygons," in 2021 IEEE 18th International Symposium on Biomedical Imaging (ISBI), 295–298, IEEE (2021).

30 U. Schmidt, M. Weigert, C. Broaddus, et al., "Cell detection with star-convex polygons," in Medical Image Computing and Computer Assisted Intervention–MICCAI 2018: 21st International Conference, Granada, Spain, September 16-20, 2018, Proceedings, Part II 11, 265–273, Springer (2018).

31 A. Khalil, Etude expérimentale d'un procédé de cristallisation en émulsion huile dans eau: Application au distéarate d'éthylène glycol. PhD thesis, Université Claude Bernard-Lyon I (2011).

32 R. Schneider and W. Weil, Stochastic and integral geometry, Springer Science & Business Media (2008).

33 S. Chiu, D. Stoyan, W. Kendall, et al., Stochastic geometry and its applications, John Wiley & Sons (2013).

34 C. Tuna, B. Mirmahboub, F. Merciol, et al., "Component trees for image sequences and streams," Pattern Recognition Letters **129**, 255–262 (2020).

35 M. A. G. de Carvalho, A. L. da Costa, A. C. B. Ferreira, et al., "Image segmentation using component tree and normalized cut," in 2010 23rd SIBGRAPI Conference on Graphics, Patterns and Images, 317–322, IEEE (2010).

36 J. C. Russ and R. T. Dehoff, Practical stereology, Springer Science & Business Media (2012).

37 L. Theodon, C. Coufort-Saudejaud, and J. Debayle, "Grape: A stochastic geometrical 3d model for aggregates of particles with tunable 2d morphological projected properties," Image Analysis and Stereology **42**(1), 1–16 (2023).

List of Figures

5 Original image on the left, background-adjusted image in the center, and contrast-adjusted image on the right.

6 Images of Adipic Acid crystals and their binarizations.

7 Two image sequences extracted from a video of Adipic Acid crystallization. These sequences are centered at a time $t_0 = 9\,min$ and have respective increments of $2\,s$ and $0.04\,s$ seconds (the camera's sampling frequency is $0.04\,s$). It is noteworthy that the portion of aggregates adhering to the air gap (highlighted in blue) evolves at a much slower rate compared to the rest of the aggregates.

8 Images from a segmented video, depicting only parts $C^{(t)}$ and $D^{(t)}$. In blue, the glued aggregates, and in green, the fully detected moving aggregates.

9 Critical cases with excessive air gap clogging result in poor segmentation of the glued part and a spatial support too constrained for accurate moving aggregate detection.

10 Distribution histograms of the maximum Feret diameter over time, for a video of Adipic Acid crystallization. The Feret's diameters unit is in pixels length (according to our spatial resolution 1 pixel $= 2\mu m$).

11 Example of the evolution of the glued part at three time points from a video of Adipic Acid crystallization.

12 llustration of the aggregate tracking rule and the corresponding connected component tree. Here, three aggregates are tracked: aggregate (A) is tracked during the period $[t_0, t_3]$, aggregate (B) during $[t_0, t_1]$, and aggregate (BCD) during $[t_2, t_3]$.

13 Evolution of the diameter of the different aggregates adhered to the gap followed during their respective periods (each curve corresponds to the tracking of an aggregate). The diameters unit is in pixels length (according to our spatial resolution 1 pixel $= 2\mu m$).